INL/JOU-21-63562-Revision-0

A Molecular Dynamics Survey of Grain Boundary Energy in Uranium Dioxide and Cerium Dioxide

November 2021

Yongfeng Zhang, Evan Hansen, Tim Harbison, Sean Masengale, Jarin French, Larry K Aagesen Jr

Changing the World's Energy Future

INL is a U.S. Department of Energy National Laboratory operated by Battelle Energy Alliance, LLC

INL/JOU-21-63562-Revision-0

A Molecular Dynamics Survey of Grain Boundary Energy in Uranium Dioxide and Cerium Dioxide

Yongfeng Zhang, Evan Hansen, Tim Harbison, Sean Masengale, Jarin French, Larry K Aagesen Jr

November 2021

Idaho National Laboratory
Idaho Falls, Idaho 83415

http://www.inl.gov

Prepared for the
U.S. Department of Energy
Under DOE Idaho Operations Office
Contract DE-AC07-05ID14517

A Molecular Dynamics Survey of Grain Boundary Energy in Uranium Dioxide and Cerium Dioxide

Yongfeng Zhang[1,2*], Evan D. Hansen[3*], Tim Harbison[3], Sean Masengale[1], Jarin French[4], and Larry Aagesen[2]

[1]Engineering Physics Department, University of Wisconsin-Madison

[2]Computational Materials and Mechanics, Idaho National laboratory

[3]Department of Physics, Brigham Young University - Idaho

[4]Department of Materials Science and Engineering, Virginia Polytechnic Institute and State University

Abstract

Uranium dioxide (UO_2) is the primary fuel material that is used in current nuclear reactors. As one of the most fundamental material parameters, grain boundary (GB) energy strongly influences many fuel properties, and the influences depend on the characters and properties of individual GBs. Using molecular dynamics simulations, a high throughput survey of GB energy in UO_2 was carried out for the purpose of elucidating the roles of GB geometry such as misorientation and inclination, as well as the bonding nature of UO_2, in affecting GB energy. GB energies in CeO_2 were calculated as well for comparison with UO_2 to investigate the generality of GB energy anisotropy in fluorite phase oxides. The results show significant GB energy anisotropy in both UO_2 and CeO_2 that is associated with the cubic symmetry of the fluorite structure. More interestingly, the GB anisotropy is found to be dependent not only on the crystal structure, but also the ionic bonding. As such, the GB energy anisotropy in fluorite oxides has significant differences compared with that in fcc metals. The data obtained and the increased knowledge on GB anisotropy will facilitate GB engineering for nuclear fuels with improved properties.

*To whom correspondence should be sent: yzhang2446@wisc.edu and Evan_Hansen@byui.edu

1. Introduction

Nuclear energy provides an essential contribution to the baseload, carbon-free electricity in the world energy portfolio. An imperative of working with nuclear fuels is preserving the integrity of fuel and cladding to prevent fission products and fuel materials from contacting and contaminating the coolant. During fuel operation, the fuel microstructure evolves, causing degradation of fuel thermomechanical properties and limiting the maximum burnup of fuel pins. Safe and stable reactor operation is achieved by fuel replacement at frequencies determined by extensive and expensive burnup test programs seeking to maximize lifetime of fissionable materials while maintaining mechanical and thermal properties of the fuel. It is of both scientific merit and technological importance to accurately predict and extend fuel lifetime, and this task centers on understanding the fuel microstructure and its evolution because of its role in determining thermomechanical properties. Critical to understanding fuel microstructure evolution is the properties and impact of grain boundaries (GBs) [1].

Crystalline materials in real applications are usually polycrystalline with numerous grains. Each grain has a unique crystal orientation that differs from its immediate neighbors. The discontinuity in crystal orientation from one grain to another is accommodated by GBs. The character and the properties of a GB depend on the orientation differences (i.e., misorientation) and the terminating crystal planes of its two neighboring grains (i.e., inclination), and such a dependence is referred to as GB anisotropy. Understanding GB anisotropy is essential for GB engineering, which seeks to improve material properties by purposely controlling the densities and characters of various GBs [2].

Most nuclear fuels in current reactors are made of UO_2 with a grain size of about 10 microns [3]. The grain morphology critically impacts the fuel properties. For instance, the thermal conductivity of UO_2 increases with decreasing GB density [4,5] due to increasing grain size, and the thermal resistance of a given GB depends on its character as indicated by results from the surrogate material CeO_2 [6]. The fracture toughness of UO_2 also increases with increasing grain size [7], and again, different GBs may exhibit different resistance to fracture, as quantified by the cleavage energy needed for intergranular fracture propagation [8]. Two other critical issues regarding fuel performance, fission gas bubble swelling and fission gas release, also depend strongly on grain size and GB character [9]. It has been widely accepted that, fission gas release occurs by the formation of percolation paths for gas atoms along GBs that have high formation energies and favor gas bubble formation. Large grain size has been shown to be effective in reducing swelling and fission gas release from the fuel at a given burnup [10]. The dependence of fuel performance on grain size is related to a fundamental GB property - GB energy, which is the driving force for grain growth that increases grain size, and many aspects of the dependence on GB character originate from GB energy anisotropy. For example, a positive correlation between GB thermal resistance and GB energy in CeO_2, which is a commonly studied surrogate ceramic for UO_2, has been suggested by molecular dynamics (MD) simulations [6]. Also, the cleavage energy for intergranular fracture in UO_2 has been shown to decrease with increasing GB energy [11,12]. The percolation paths for gas release are likely comprised of high energy GBs which favor gas bubble

nucleation and growth [13]. Therefore, there is a critical need to understand GB energy and its anisotropy in UO_2.

GBs in common metals such as fcc and bcc metals have been extensively studied [14–18], with the GB energy anisotropy well established [19]. Studies of GB energy anisotropy have also been conducted for rock-salt phase ceramics such as MgO [20] and fluorite phase ceramics such as yttrium stabilized zirconia (YSZ) [21]. These studies have led to several important findings. First, GB energy anisotropy is largely determined by the crystal structure. Consequently, isostructural materials may share similar anisotropy in GB energy. For instance, the GB energies in fcc metals can be described using a universal model, with a scaling factor for each metal [14], and so is true for bcc metals [18]. Second, there may exist a strong correlation between GB energy and GB plane(s), the terminating surfaces of the two neighboring grains separated by a GB. Related to that, it was suggested that the GB energy anisotropy follows the anisotropy in surface energy [22], which allowed for derivation of GB energies from surface energies, particularly for GBs with large misorientations. For GBs with small misorientation, dislocation based theoretical models such as the Read-Shockley model [23] were found to give a reasonable prediction of GB energy [22]. Last but not least, it was recently found that there is an inverse correlation between GB energy and GB population in systems that have been thermally equilibrated such as MgO [20] and UO_2 [11].

There is, however, a gap in the knowledge of GB energy anisotropy for UO_2, or fluorite phase oxides in general, mainly due to the insufficiency of data. As far as we know, there has been no direct experimental measurement of GB energies in UO_2, while important information on the character and population of different GBs in polycrystalline UO_2 have been obtained by electron-back-scattering-diffraction (EBSD) [11,24,25]. The GB energies data in UO_2 are mostly from atomistic calculations, primarily molecular dynamics (MD) simulations [8,11,24,26–31]. For the high computation cost needed, first-principle based density functional theory (DFT) calculations have rarely been applied for GBs in UO_2 [24]. Previous MD calculations have usually considered a few GBs, and the interatomic potentials used are often different across studies. By far, the most extensive calculations are done by Bourasseau et al. [11] and Ksibi et al. [31], with 26 and 34 GBs studied, respectively. In particular, coupled with EBSD results, an inverse correlation between GB energy and GB population (represented by the length fraction) was established by Bourasseau et al. [11], similar to that in fcc metals and MgO [22]. Still, more data are needed in a broader range of misorientation and inclination to improve the understanding of GB energy anisotropy in UO_2, and this is the objective of the present work.

This work surveys GB energy anisotropy in UO_2 and CeO_2 using MD simulations. The energies of 230 GBs in UO_2 were calculated to provide a data set with a broad range of misorientations and inclinations. As there has been no systematic data on GB energies in fluorite ceramics, the results are discussed in reference to fcc metals and ceramics such as MgO, CeO_2 and YSZ, to elucidate the roles of crystal structure and the bonding nature in affecting GB energy. For UO_2, the trends in GB anisotropy are found to have much in common for the four different interatomic potentials utilized, although the exact energy of a given GB depends on the choice of potential.

2. Methodology

2.1 GB notation

A brief introduction of GB notation is provided to help with the description of the simulation setup and the presentation of results. From a macroscopic point of view, five degrees of freedom (DOFs) are needed to fully define a GB, and the five DOFs can be defined in different ways. A commonly used approach combines three DOFs for misorientation and two others for inclination, as used in Bulatov et al. [14] and shown in the schematic in Fig.1. The two neighboring grains intersecting at a GB can be oriented with respect to each other by a rotation about an axis $\hat{m}$ (2 DOFs), with an angle ξ (1 DOF). The rotation axis is usually denoted by the Miller index of a crystal orientation, e.g., <111>; it has two DOFs because only the direction is of interest. The ($\hat{m}$, ξ) pair (3 DOFs) defines the misorientation. A GB can then be created by cutting the two grains with a common plane – the GB plane – defined by its normal $\hat{z}$ (2 DOFs), which represents the inclination. Note that for asymmetric GBs, the GB plane may correspond to two different crystal planes in the two neighboring grains, and either can be used to define the GB plane. Two special GB categories, the pure *twist* and *tilt* GBs, include all GBs that can be defined by special choices of the angle (ϕ) between the rotation axis ($\hat{m}$) and the GB normal ($\hat{z}$): ϕ is 0° for twist (Fig.1(a)), 90° for tilt (Fig.1(b)).The angle ϕ is between 0° and 90° for mixed GBs with both twist and tilt characters (Fig. 1(c)). A further classification can be done to divide the special tilt GBs into *symmetric* (STGB) and *asymmetric* (ATGB) tilt GBs. The misorientation angle between the two neighboring grains can be created by rotation about $\hat{z}$ from the same reference GB in opposite directions with angles θ_1 and θ_2 (Fig.1(b)), respectively, so that the misorientation angle is $\xi = \theta_1 - \theta_2$ (considering the opposite sign). Another angle defined as $\eta = \theta_1 + \theta_2$, termed as the *asymmetry* angle here, measures the deviation of an ATGB from an STGB with the same rotation axis and angle. A tilt GB with $\eta = 0$ is an STGB, and is an ATGB otherwise. The above description of GBs is subject to symmetry operations (rotations that transform a crystal to its symmetric equivalents) that is given by the crystal symmetry, based on which the GB planes can be grouped into fundamental zones [32]. For instance, a given GB may be defined equivalently by different combinations of ($\hat{m}$, ξ, $\hat{z}$), which can be converted from one to another by symmetry operations. Because of the 5 macroscopic DOFs needed to specify a GB, GBs are often referred to as five dimensional (5D). Partially fixing the DOFs results in lower dimensional subsets of GBs. For instance, the STGBs and twist GBs with a known rotation axis are referred to as 1D GB sets because only one DOF, the misorientation angle ξ, is allowed to vary. The ATGBs with a given rotation axis are thus 2D because the asymmetry angle η, can vary as well. The mixed GBs with a given rotation axis are 3D as the angle ϕ becomes independent as well.

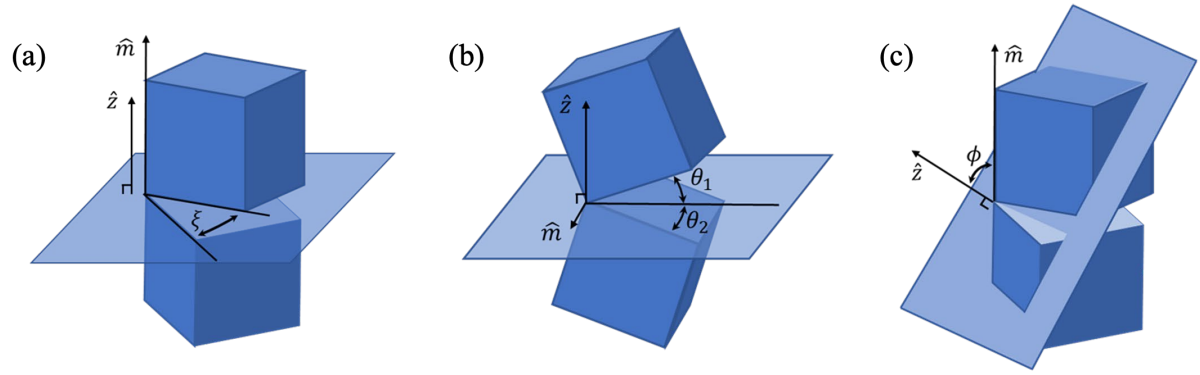

Figure 1. Bicrystal schematics showing (a) pure twist, (b) pure tilt, and (c) mixed GBs. The lattices for two grains forming a bicrystal are shown as cubes. The GB normal, $\hat{z}$, and the rotation axis, $\hat{m}$, parallel each other for pure twist in (a), perpendicular to each other for pure tilt in (b), and form an angle between 0° and 90° for mixed GBs in (c).

Another commonly used descriptor for GB character is the Σ number, which comes from the coincident site lattice (CSL) theory [33]. The Σ number is an integer, defined as the inverse of the fraction of lattice sites that are coincident in the two neighboring grains, e.g., the top and bottom grains in Fig. 1 after the rotation, independent of the inclination of the GB they occlude. Accordingly, the Σ number concerns only the misorientation without considering the inclination. It can be related to the GB planes only when a specific set of GBs, for example, twist or STGBs, is specified. In spite of its wide use, the Σ number was found not a good descriptor of GB energy [22], because each Σ number corresponds to numerous GBs with different GB energies.

In this work, the energy of a total of 230 GBs in UO_2 are calculated, with a focus on GBs with the rotation axis being a low-index crystal orientation, <1 0 0>, <1 1 0> or <1 1 1>, including 1D twist and STGBs, as well as ATGBs and mixed GBs. 12 high-angle, asymmetric GBs are also calculated to represent random GBs. These GBs are selected to cover the misorientation and inclination space and have been used as the bases to construct a five-dimensional (5D) GB energy model following that for fcc metals developed by Bulatov et al. [14]. The fitted model is tested using the results for <210> twist and STGBs. The numbers of GBs used in the MD calculations are summarized in Table 1. The energies for the 1D GBs in CeO_2 are also calculated.

Table 1: Number of UO_2 GBs per boundary type used in the MD calculations

Axis / **Misorientation**	Twist	Symmetric Tilt	Asymmetric Tilt	Mixed
<100>	14	17	14	10
<110>	18	29	20	17
<111>	18	12	15	13
<210>	13	9	0	0
Random GBs		12		

2.2 GB construction

A bicrystal structure similar to those used in previous studies [8] is used in the MD simulations for GB energy. As shown in Fig.2, the simulation cell contains a top and a bottom grain, with the GB normal along the *Z* direction. Both grains are stoichiometric, single-crystal UO_2 of the fluorite phase, with their crystal orientations along the three principal axes, X, Y and Z, described by two matrices, P and Q, respectively. Periodic boundary conditions are applied along all three principal axes after the two grains are stacked along the Z direction. Note that with periodicity there are two GBs created, one between the grains and the other at the cell boundary perpendicular to Z. The dimensions of the simulation cells vary depending upon the GBs being simulated. The dimension along each principal axis is at least twice of the periodic length of the corresponding crystal orientation and at least twice the cutoff of the interatomic interaction distance to avoid direct

interaction of an atom with its periodic image. The periodic length along the <h k l> direction is $\sqrt{h^2 + k^2 + l^2}$ multiplied by the lattice constant, a_0. We further kept the grain size, which is the distance between two parallel GBs, above 5 nm to minimize GB-GB interactions.

For symmetric GBs such as twist and STGBs, the top and bottom grains share exactly the same dimensions along their particular coordinate axes. However, for asymmetric GBs, the periodic lengths of the two grains along the same principal axis may differ from one grain to another because of the different crystal orientations. With finite-sized simulation cells, the dimensions of the two grains in the X or Y axis may not be commensurate with each other exactly, and an in-plane *mismatch* strain becomes unavoidable when the periodic boundary condition is applied. To minimize this artifact, the dimensions of both grains are varied by varying the numbers of unit cells they contain until the mismatch is below 0.5%. Consequently, the error induced by the strain energy becomes negligible.

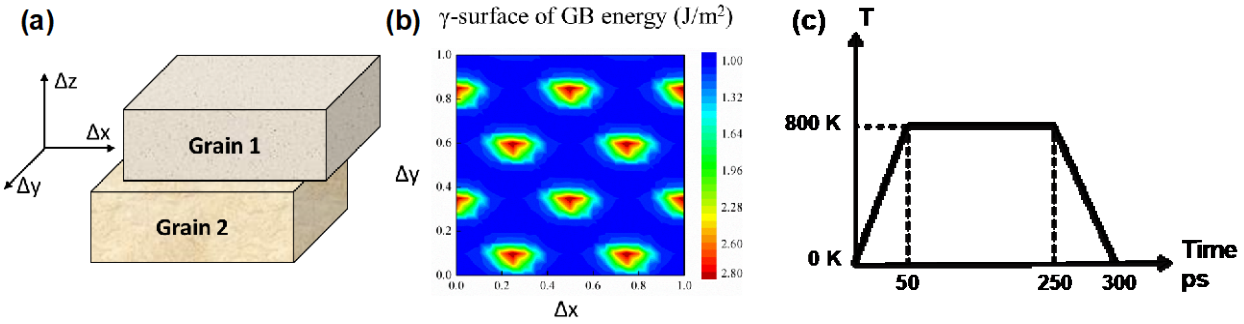

Figure 2. (a) Schematic of a bicrystal model for GBs with an in-plane translation for γ-surface mapping. (b) The GB energy from γ-surface mapping for the intrinsic Σ3 twin boundary in UO_2. (c) The annealing procedure to relax the GB structure.

2.3 MD calculations

A two-step procedure is used to compute the GB energy. In the first step, a γ-surface mapping [24] is carried out at 0 K to account for the three microscopic DOFs of GBs, i.e., the relative translation between the top and the bottom grains along the three principal axes, as shown in Fig. 2(a). Specifically, the top grain is shifted in reference to the bottom grain in incremental steps up to the displacement shift complete (DSC) vectors, to identify the relative translation that gives the lowest total energy. The DSC vectors are the smallest relative translations that preserve the GB structure. The translation along Z is taken care of by a stress-free boundary condition. The step sizes used along X and Y depend on the lengths of the DSC vectors, with a maximum step size of 0.5 Å, depending on the unit periods in the GB plane. In general, more than a thousand calculations are needed to map the microscopic DOFs for each individual GB. The lowest energy GB from γ-surface mapping is regarded as the stable GB structure at 0 K.

In the second step, the 0 K GB configuration is annealed using the procedure shown in Fig. 2(c) to further relax the GB structure since the 0 K minimization may relax the system into a local instead of the global energy minimum. The system temperature is raised to 800 K in 50 ps, kept at 800 K for 200 ps, and then quenched down to 0 K in 50 ps. The annealing temperature is the same

as used in Nerikar et al. [24], but is lower than those used in Bourasseau et al. [11], Chen et al.[27], and Williams et al. [29]. A temperature that is too low may be insufficient to relax the GB structures, while a temperature that is too high may relax the GBs into high-temperature structures which are different from the low temperature structures. Given the short MD simulation time, the GB structures may not be fully relaxed regardless of the annealing temperature used. The total energy of the quenched cell, E_t, is used to calculate the GB energy, ε, using Eq. 1.

$$\varepsilon = \frac{E_t - E_0}{2A} \qquad (1).$$

Here E_0 is the energy of a defect free system with the same numbers of U and O ions in the fluorite phase, and A is the GB area in the bicrystal (note there are two GBs). Both the 0 K and the annealed GB energies are calculated to show the effect of annealing. In addition to the GB energy, the excess GB volume is also calculated for 1D GBs using:

$$\delta V_b = \frac{V_t - V_0}{2A} \qquad (2).$$

Here V_t is the volume of the bicrystal cell, V_0 is the volume of a defect free system with the same numbers of U and O ions in the fluorite phase.

Four interatomic potentials, Basak [34], Morelon [35], Yakub [36] and Cooper [37], are used to describe the interatomic interaction, with Basak chosen as the primary one to demonstrate the GB energy anisotropy. Among these four, the Basak potential has been commonly used for thermomechanical properties of bulk UO_2. And the local oxygen rearrangement near a [100] Σ5 STGB predicted by the Basak potential has been benchmarked against DFT calculations in the literature [24]. The Cooper potential was recently shown to give a reasonable correlation between energy and GB population in UO_2 [11]. Two other commonly used potentials, Morelon and Yakub, are used to further elucidate the dependence of the results on the choice of interatomic potential. The Yamada potential [38] is also tested, but was found to give disordered GBs and unrealistic-sometimes negative-GB energies. We note that in the literature dozens of interatomic potentials have been developed for different properties of UO_2 [39,40], none of which have been systematically benchmarked upon GB properties. To improve the computation efficiency, the coulomb interaction between ions is computed using the Wolf summation [41] with a cutoff radius of $2a_0$ and a damping constant of $1.5/a_0$, which has been shown to be suitable for UO_2 [42]. All simulations are carried out using the LAMMPS simulation package [43] which has the Wolf summation built in. The adaptive timestep is used, with a minimum of 0.1 fs and a maximum of 2.5 fs, with a maximum atomic displacement of 0.1 angstrom per timestep. For all calculations, a periodic, stress-free boundary condition is applied along all three directions. The thermostat and barostat as built in LAMMPS [44] is used to control temperature and pressure. The Ovito software [45] is used while presenting the atomic configurations.

To generalize our UO_2 results to fluorite phase oxides, the energies of the 1D GBs in Table 1 in CeO_2 are also calculated. The same procedure as used for UO_2 GBs are used for CeO_2. The Gotte potential [46] is used for the interatomic interaction. The original core-shell potential is simplified as a rigid-ion potential for computation efficiency following Chernatynskiy et al. [6], where the

rigid-ion version of the Gotte potential has been shown to give reasonable results for the correlation between GB energy and GB Kapitza resistance to thermal conduction.

3. Results

In presenting the results, we focus on the results obtained with the Basak potential. The dependence of the results on interatomic potentials will be discussed in Section 4. The calculated GB energies for 230 UO_2 GBs and 118 1D CeO_2 GBs are given in the supplementary material "UO2&CeO2_GB_energy.csv". The GBs are described by the crystal orientations along the principal axes for the top and the bottom grains, with the GB plane perpendicular to the Z direction. The GB energies obtained with the Basak potential are further used to fit the analytical models proposed by Bulatov et al. for fcc metals [14] adapting the Matlab code shared in the same work. This adaptation is motivated by the fcc U sublattice in UO_2 and by the similar dependence of GB energies on the misorientation angle observed between UO_2 and fcc metals. For completeness, the equations proposed by Bulatov et al. [14] are re-introduced here with some minor corrections. The resulting fitting parameters are listed in Table A1 in the Appendix.

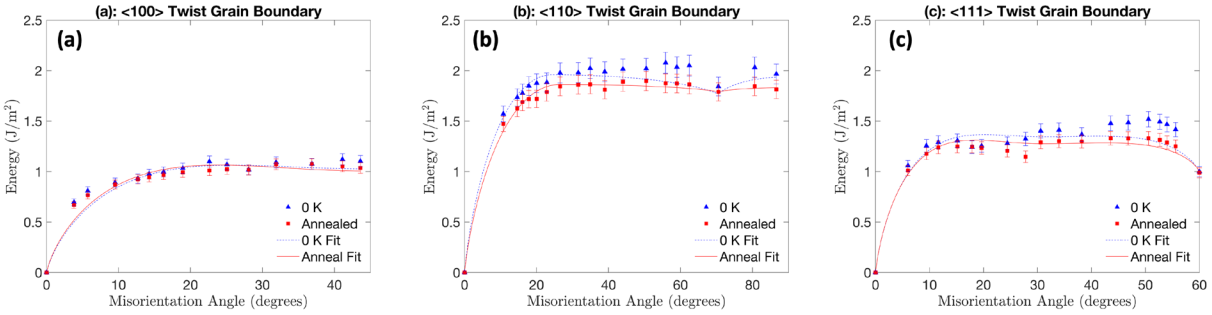

Fig. 3. Energies of (a) <100>, (b) <110>, and (c) <111> twist GBs as functions of misorientation angle, ξ. The lines are 1D Bulatov-Reed-Kumar (BRK) functions fitted to MD results obtained using the Basak potential with (red square) and without (blue triangle) annealing. 5% errors are added to the MD data following Bulatov et al. [14].

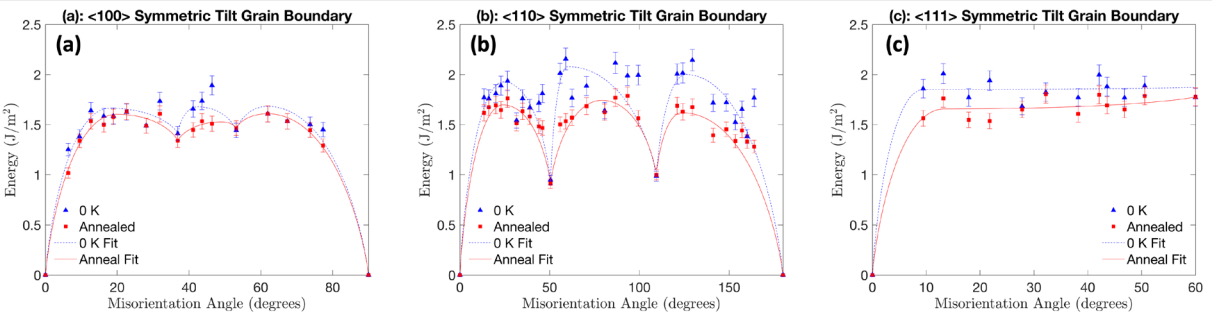

Fig. 4. Energies of (a) <100>, (b) <110>, and (c) <111> STGBs as functions of misorientation angle, ξ. The lines are 1D Bulatov-Reed-Kumar (BRK) functions fitted to MD results obtained using the Basak potential with (red square) and without (blue triangle) annealing. 5% errors are added to the MD data following Bulatov et al. [14].

3.1 1D and 2D GBs in UO_2

In Fig. 3, the GB energies, ε, are plotted as a function of misorientation angle for 1D <100>, <110> and <111> twist GBs. The GBs energies for <100>, <110> and <111> STGBs are shown in Fig. 4. For each MD data point, a 5% uncertainty is added following Bulatov et al. [14]. The GB energies for the 1D GBs are fitted to the 1D Bulatov-Reed-Kumar (BRK) functions, which were originally constructed for fcc metals [14]. In the 1D BRK function, the entire range of misorientation angle, ξ, is divided into segments separated by cusps in the GB energy. In each segment, the GB energy is described by a Reed-Shockley-Wolf (RSW) function, f_{RSW}, which was initially developed based on the dislocation model for low angle GBs by Reed and Shockley [23] and later extended for high-angle GBs by Wolf et al. [47]. The 1D BRK function and the RSW function are given in Eqs. (3) and (4), respectively:

$$\varepsilon(\xi) = \varepsilon(\xi_{min}) + \big(\varepsilon(\xi_{max}) - \varepsilon(\xi_{min})\big) f_{RSW}(\xi, a) \quad (3).$$

$$f_{RSW}(\xi, a) = sin\left(\frac{\pi}{2}\frac{\xi-\xi_{min}}{\xi_{max}-\xi_{min}}\right)\left(1 - a\, log\, sin\left(\frac{\pi}{2}\frac{\xi-\xi_{min}}{\xi_{max}-\xi_{min}}\right)\right),\ \xi_{min} \le \xi \le_{max} \quad (4).$$

Here, $\varepsilon(\xi_{min})$ is the GB energy at a cusp located at the misorientation angle ξ_{min}. The same cusp locations as used for fcc metals [14] are used for UO_2 considering that the U sublattice in UO_2 is fcc. Indeed, the calculated GB energies in UO_2 from MD show cusps at these locations as well. $\varepsilon(\xi_{max})$ is the peak GB energy within a given segment obtained at the misorientation angle ξ_{max}; both $\varepsilon(\xi_{max})$ and ξ_{max} are fitting parameters. The RSW function goes from 0 to 1 from a cusp to a peak in GB energy. The shaping parameter, a, adjusts the shape of the RSW function and is fixed at 0.5 following Bulatov et al. [14] unless stated otherwise. The MD data with and without annealing are fitted independently, and they show similar dependence on the misorientation angle. In general, annealing leads to lower GB energies and a smaller fluctuation in the results. The good agreement between fitted and MD results indicates that the dislocation based BRK functions are applicable for UO_2, which is consistant with a recent MD study that demonstrated the dislocation structures in UO_2 GBs [12].

The energies of three 2D GB sets, the <100>, <110> and <111> ATGBs, are plotted in Fig. 5 as functions of the misorientation angle, ξ, and the asymmetry angle, η. The energies of the ATGBs are fitted to Eq. (5) for <100>, Eq. (6) for <110>, and Eq. (7) for <111>, respectively. Equation (6) differs slightly from its original form (Eq. (7) in Bulatov et al.) as the period for <110> tilt GBs should be π instead of $\frac{\pi}{2}$; the value π was used in the Matlab code shared by Bulatov et al. These models predict the energy ($\varepsilon_{hkl}^{tilt}(\xi,\eta)$) of an ATGBs with a misorientation angle ξ and an asymmetry angle η by interpolating the energies of STGBs with same (ξ) and the complementary ($\frac{\pi}{2}-\xi$) or supplementary ($\pi-\xi$) misorientation angles. We note that these models are empirical in nature, and their functional forms largely control the shape of the 2D GB energy surface, although they fit well to MD data for fcc metals [14] and for UO_2 here.

$$\varepsilon_{100}^{tilt}(\xi,\eta) = \begin{cases} \varepsilon_{100}^{stgb}\left(\frac{\pi}{2}-\xi\right)+\left(\varepsilon_{100}^{stgb}(\xi)-\varepsilon_{100}^{stgb}\left(\frac{\pi}{2}-\xi\right)\right)\left(1-\frac{2\eta}{\pi}\right)^{p}, & \varepsilon_{100}^{stgb}(\xi)>\varepsilon_{100}^{stgb}\left(\frac{\pi}{2}-\xi\right) \\ \varepsilon_{100}^{stgb}(\xi)+\left(\varepsilon_{100}^{stgb}\left(\frac{\pi}{2}-\xi\right)-\varepsilon_{100}^{stgb}(\xi)\right)\left(\frac{2\eta}{\pi}\right)^{p}, & \varepsilon_{100}^{stgb}(\xi)\le\varepsilon_{100}^{stgb}\left(\frac{\pi}{2}-\xi\right) \end{cases} \quad (5).$$

$$\varepsilon_{110}^{tilt}(\xi,\eta)=\begin{cases}\varepsilon_{110}^{stgb}(\pi-\xi)+\left(\varepsilon_{110}^{stgb}(\xi)-\varepsilon_{110}^{stgb}(\pi-\xi)\right)f_{RSW}\left(1-\frac{\eta}{\pi},a_{110}^{atgb}\right), & \varepsilon_{110}^{stgb}(\xi)>\varepsilon_{110}^{stgb}(\pi-\xi)\\ \varepsilon_{110}^{stgb}(\xi)+\left(\varepsilon_{110}^{stgb}(\pi-\xi)-\varepsilon_{110}^{stgb}(\xi)\right)f_{RSW}\left(\frac{\eta}{\pi},a_{110}^{atgb}\right), & \varepsilon_{110}^{stgb}(\xi)\le\varepsilon_{110}^{stgb}(\pi-\xi)\end{cases} \quad (6).$$

$$\varepsilon_{111}^{tilt}(\xi,\eta)=\begin{cases}\varepsilon_{111}^{stgb,max}f_{RSW}(\xi,0.5), & 0\le\xi\le\xi_{111}^{tilt,max}\\ \varepsilon_{111}^{stgb,\Sigma3}(\eta)+\left(\varepsilon_{111}^{stgb,max}-\varepsilon_{111}^{stgb,\Sigma3}(\eta)\right)f_{RSW}(\xi,0.5), & \xi_{111}^{tilt,max}<\xi\le\frac{\pi}{3}\end{cases} \quad (7).$$

where

$$\varepsilon_{111}^{stgb,\Sigma3}(\eta)=\varepsilon_{111}^{tilt,\Sigma3,max}+\left(\varepsilon_{111}^{atgb,\Sigma3,max}-\varepsilon_{111}^{stgb,\Sigma3}\right)f_{RSW}(\eta,0.5),\quad 0<\eta<\frac{\pi}{2\lambda} \quad (8).$$

In the above equations, p, a_{110}^{atgb}, $\varepsilon_{111}^{stgb,max}$, $\varepsilon_{111}^{stgb,\Sigma3}$, $\varepsilon_{111}^{tilt,\Sigma3,max}$, $\varepsilon_{111}^{atgb,\Sigma3,max}$ are fitting parameters.

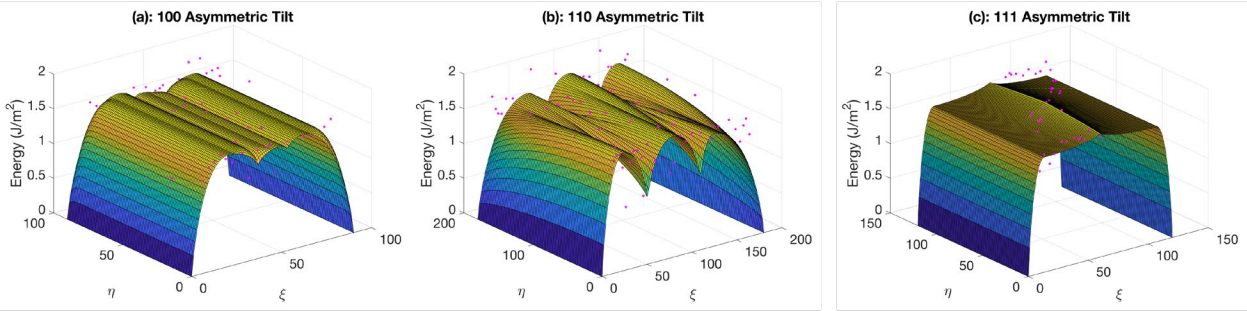

Figure 5. GB energies of (a) <100>, (b) <110> and (c) <111> ATGBs as functions of the misorientation angle ξ and the asymmetry angle η. The symbols are from MD and the surface plots are fitted using the 2D BRK functions given in Eq. (5)-(8).

3.2 5D GB model for UO_2

Encouraged by the good fitting results in Figs 3-5, an attempt is made to fit a 5D GB energy model for UO_2 following the model for fcc metals in Bulatov et al. [14]. A hierarchical fitting procedure is adopted. First, the random GB energy, ε_{RGB}, is obtained by averaging the results for all UO_2 GBs calculated except the <210> twist and STGBs. The second step fits the 1D GB sets as shown in Figs. 3 and 4. The third step fits the <100>, <110> and <111> 2D ATGBs using Eqs. (3)-(8), as shown in Fig.5. In step four, three 3D scaffolding sets, the <100>, <110> and <111> mixed GBs, are fitted, using Eq.(9) for <100> and <110> and Eq.(10) for <111> mixed GBs, respectively.

$$\varepsilon_{hkl}(\xi,\eta,\phi)=\varepsilon_{hkl}^{twist}(\xi)\left(1-\frac{2\phi}{\pi}\right)^{p_{hkl}^1}+\varepsilon_{hkl}^{tilt}(\xi,\eta)\left(\frac{2\phi}{\pi}\right)^{p_{hkl}^2} \quad (9).$$

$$\varepsilon_{111}(\xi,\eta,\phi)=\varepsilon_{111}^{twist}(\xi)\left(1-\alpha\frac{2\phi}{\pi}+(\alpha-1)\left(\frac{2\phi}{\pi}\right)^2\right)+\varepsilon_{111}^{tilt}(\xi,\eta)(\alpha\frac{2\phi}{\pi}-(\alpha-1)\left(\frac{2\phi}{\pi}\right)^2) \quad (10).$$

The last step fits arbitrary 5D GBs using the MD data for random GBs. In the Bulatov model, a 5D GB is approximated by best-matching GBs in the three 3D scaffolding sets, the <100>, <110> and <111> mixed GBs, and its energy is taken as the weighted average of the energies of those best-matching GBs, by

$$\varepsilon=\frac{1+\sum w_{hkl}(d_3)\varepsilon_{hkl}(\xi,\eta,\phi)}{1+\sum w_{hkl}(d_3)}\varepsilon_{RGB} \quad (11).$$

In Eq.(11), d_3 is the *distance* between the targeting GB and one of its best-matching GBs in the misorientation space; the procedure of calculating d_3 is provided in Bulatov et al. [14]. The corresponding weighting function is given by:

$$w_{hkl}(d_3) = \frac{w_{hkl}^0}{sin\frac{\pi d_3}{2d_{hkl}^{max}}(1-\frac{1}{2}\log(sin\frac{\pi d_3}{2d_{hkl}^{max}}))-1} \qquad (12).$$

The fitting is carried out by minimizing the mean square deviation of the fitted GB energies from the MD data. The resulting 43 fitting parameters for UO_2 are listed in Table A1 in the Appendix.

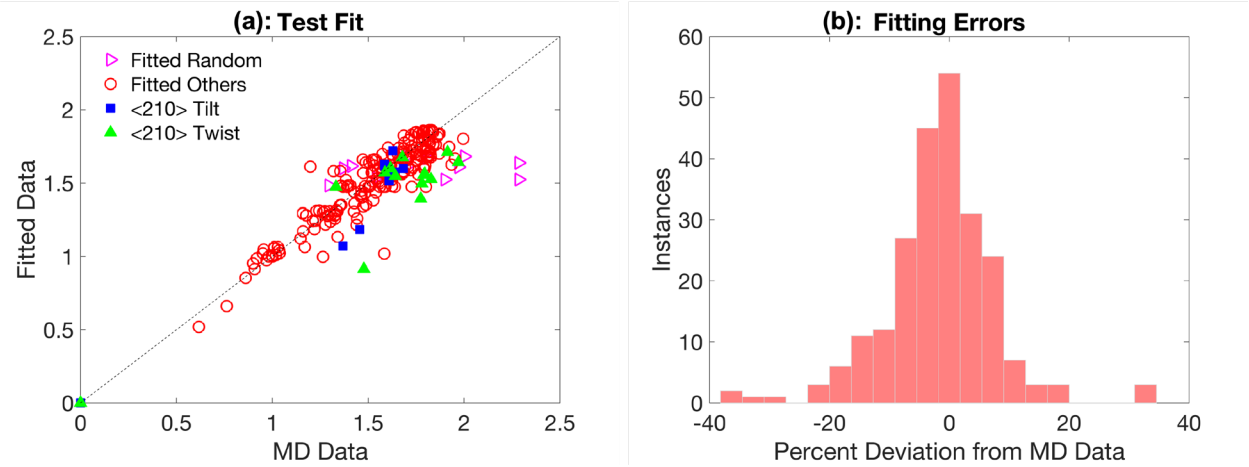

Figure 6. (a) Fitted GB energies versus MD data and (b) fitting errors shown by distribution of percent deviation of fitted GB energies from MD data. In (a), the GB energies used in the fitting are shown by open symbols, and a dash line $y = x$ is added to help visualization. As shown in (b), most fitting errors are within 20%.

The fitted 5D model can be used to estimate the energy for any arbitrary GBs. As inputs, the matrices P and Q describing the crystal orientations of the top and bottom grains are needed. These matrices are converted to rotation matrices that rotate the Z axes (GB normal) to [100], for use in the Matlab code (GD5DOF.m) shared by Bulatov et al. [14] to predict the GB energy. To test this, the energies of all GBs listed in Table 1 are recalculated based on their P and Q matrices and plotted versus the MD data. The fitting errors are computed as the percent deviation of the predicted GB energies from the corresponding MD results. The GBs used in fitting are divided into random GBs (which are high-angle, asymmetric GBs) and others. In Fig.6(a), the fitted results agree well with the MD results used in fitting, with slightly larger deviations for random GBs than for other GBs. Overall, most fitting errors are within 20%, as shown in Fig.6(b). It is also encouraging to see the reasonable agreement for <210> twist GBs and STGBs, which are not used in fitting and serve as validation data.

It should be noted that the 5D model is largely empirical. There has been no physical evidence showing the GB energy is a continuous function in the 5D space to justify the interpolation and extrapolation scheme. Second, provided such continuity exists, the interpolation and extrapolation functions used, except for the RSW function, are largely empirical. Third, it's not certain that the

model for fcc metals is transferrable to UO_2 considering the different crystal structures and bonding natures. Therefore, caution is needed when using the model to make predictions.

4. Discussion

4.1 GB energy anisotropy in UO_2

As shown in Figs. 3-5, the energies of 1D GBs in UO_2 exhibit a similar dependence on the misorientation angle to that in fcc metals, suggesting a similar GB energy anisotropy in UO_2 and in fcc metals. For all 1D GB sets, the same GB energy cusps in fcc metals are also observed in UO_2. This similarity may come from the similarity of fcc and fluorite in the crystal structures as both have cubic symmetry. Furthermore, the U sublattice follows the fcc structure. This implies the role of crystal structure in determining the GB structure and energy, consistent with Bulatov et al. [14], where the GB energies in four fcc metals are found to share the same anisotropy, with a material-specific scaling factor for each metal. The same conclusion has been reached for bcc metals by Ratanaphan et al [18]. Aside from the overall similarity, several differences are also noticed between the GB energy anisotropy in fcc metals and in UO_2.

The most notable difference is the relative GB energies among the 1D twist GB sets. In metals, GBs located on the most densely packed crystal planes, which are {111} in fcc and {110} in bcc, respectively, usually have lower energies compared to GBs on other planes. For example, with the same misorientation angle, the {111} twist GBs were found to have lower energies than {100} and {110} twist GBs in fcc Ni, Cu, Al, and Au [15] and fcc austenitic steel [48]. Similarly, in bcc Mo and Fe, with the same misorientation angle, <110> twist GBs are of much lower energy than other GBs except for the Σ3 twin on the {112} plane [18]. However, in UO_2, the {111} twist GBs, which are on the most densely packed plane in the fcc U sublattice, have higher energies than the {100} twist GBs. There has been no experimental data for UO_2 to validate this trend. In YSZ, which is also of the fluorite structure, it has been experimentally observed that GBs on the {100} plane are more common than GBs on the {111} plane [21], implying that GBs on {100} planes are of lower energy than on {111} planes. Also, as will be shown later, the same trend is observed in CeO_2 by MD calculations, suggesting that this may be general for ceramics with the fluorite structure.

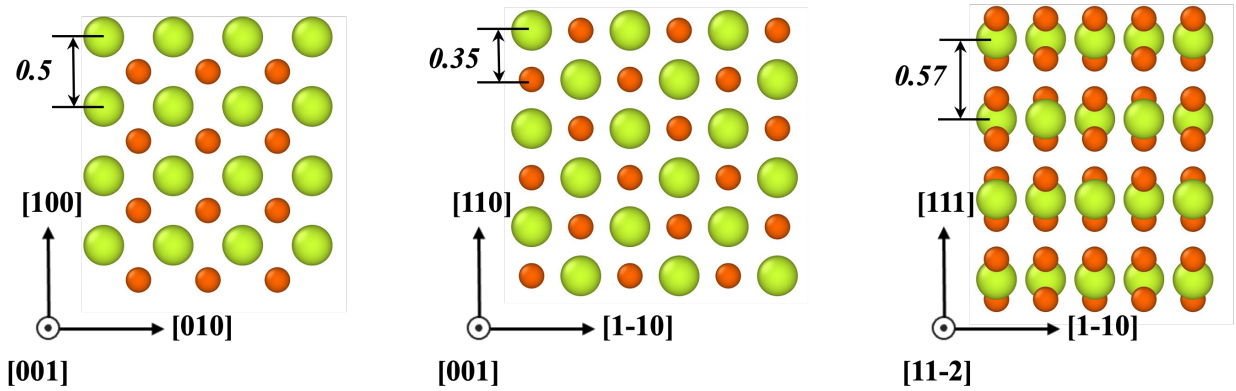

Figure 7. Single crystal UO_2 cells with the *Z* axis along (a) [100], (b) [110], and (c) [111] to show the stacking sequence and interplane distance in unit of the lattice constant, a_0. Large and small

atoms represent U and O, respectively. While {111} planes have the largest interplane distance, negatively charged O ions directly facing each other in a short distance.

This difference indicates that the GB energy anisotropy is not solely determined by the crystal structure, but also the bonding nature. The bonding nature in UO_2 has an ionic component, different from the pure metallic bonding in fcc and bcc metals. Specifically, each {111} U plane is sandwiched by two O planes, as shown in Fig. 7. The two O planes from two neighboring {111} planes directly face each other with a small separation, as shown in Fig. 7(c). Because of the interruption of the periodic distribution of ions and the short distances between O ions, the repulsion between negatively charged O ions in close distances may lead to high energies in {111} twist GBs. Similarly, O and U ions share the {110} plane, and ions of the same charge may be located near each other in a {110} twist GB, as shown in Fig. 7(b). In contrast, along <100>, O and U planes stack alternately, as shown in Fig. 7(a), so that ions with the same charge are screened by oppositely charged ions, avoiding strong repulsion when a {100} twist GB is formed. Consequently, the repulsion between ions of the same charge will cause a higher energy penalty for GBs on {111} and {110} planes than on {100} planes, leading to lower energies for GBs on {100} planes.

The positive correlation between GB energy and surface energy as observed in fcc metals and MgO [22] is absent in UO_2. It has been observed in fcc metals and MgO that GBs located on the crystal planes that give low surface energies also have low GB energies as well. As such, the surface energy can be used as an indicator for GB energies. More specifically, the GB energy, ε, can be approximated as the sum of the energies of the two surfaces that make up the GB, γ_{s1} and γ_{s2}, minus a constant term representing the bond energy between the two surfaces [20], by

$$\varepsilon = \gamma_{s1} + \gamma_{s2} - \varepsilon_b \quad (13)$$

Where ε_b was hypothesized as more or less a constant for different GBs [20]. This trend was found to hold in fcc metals [16] and in ceramic MgO [20]. However, in UO_2, the {111} surface was shown to have much lower surface energy than {100} by previous MD calculations [8,11], while the {111} twist GBs are of much higher energy than {100} twist GBs, as shown in Fig. 3. It seems that the surface energy, without being affected by the short-range repulsion between ions with the same sign of charge, still follows the general rule that surfaces on more densely packed planes have lower energy. However, such a rule is violated for GB energies, possibly due to the strong ion-ion repulsion that develops when GBs are formed.

Another minor difference noticed is that the cusps in GB energy in UO_2 are much shallower than in fcc and bcc metals. In particular, the energy of the intrinsic Σ3 twin in fcc metals represents a deep cusp in the {111} twist and the <110> STGB sets, while in UO_2 the energy of the Σ3 twin is comparable to the energies of vicinal GBs, as shown in Fig. 3(c). This is also possibly due to the ionic interaction in UO_2. Formation of GBs interrupts the periodic distribution of ions resulting in a penalty in energy that is not strongly dependent on the GB character, leading to a smoother GB energy landscape in UO_2 than in fcc metals.

4.2 Dependence on interatomic potential

Results of MD simulations depend critically on the validity of the interatomic potential used. While in the literature dozens of potentials are available for UO_2 [39,40], none were fitted or rigorously validated upon GB properties. Therefore, it is of interest to find out if the GB energy anisotropy shown in Fig. 3-5 is an artifact of using the Basak potential, by comparing the results from Basak to those from the Morelon, Yakub and Cooper potentials. To save computation time, only annealing calculations with the minimized GB configurations are done using these three potentials. The comparison is limited to the 1D twist and STGB sets. The data are available in the supplementary material "UO2&CeO2_GB_energy.csv".

In Fig. 8, the energies of the six 1D GB sets from all four potentials are plotted as functions of misorientation angle. All four potentials show similar trends regarding the dependence of GB energy on the misorientation angle and on the GB plane. For all four potentials, the <100> twist GBs have lower energies than the <111> and the <110> twist GBs at the same misorientation angle. These results indicate that the anisotropy obtained from the MD calculations is likely independent of the choice of potential.

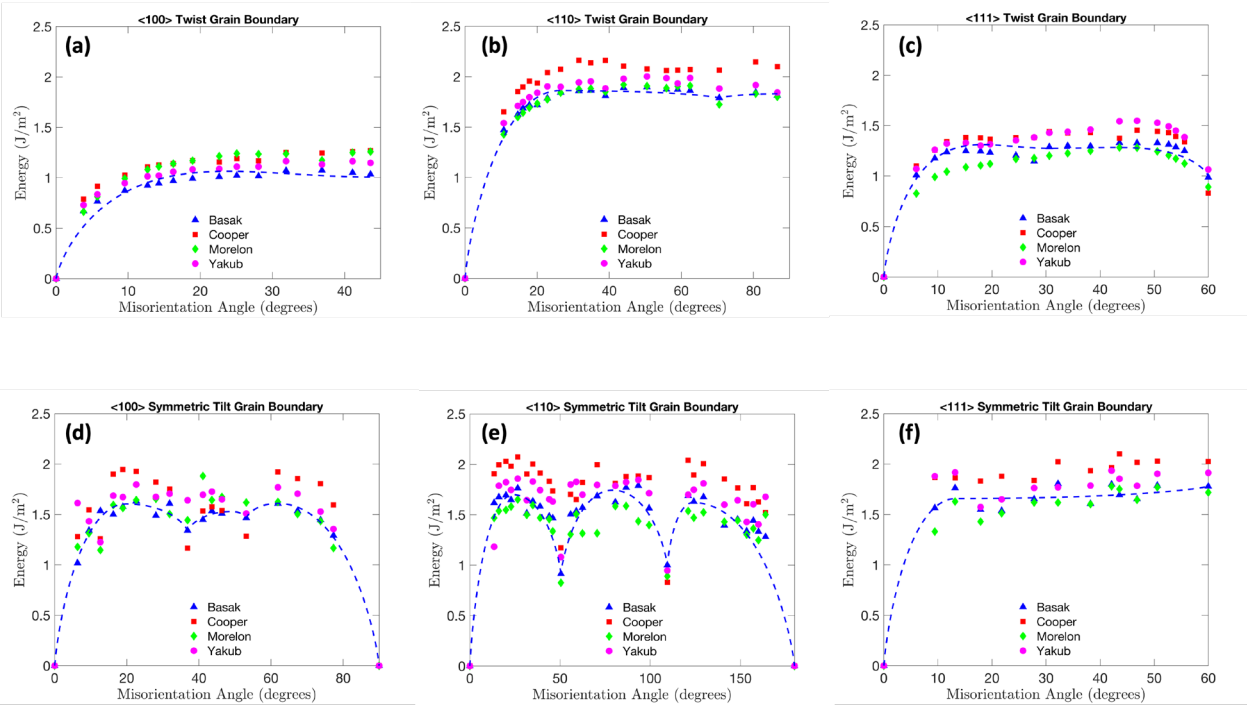

Figure 8. GB energies for (a) <100> twist, (b) <110> twist, (c) <111> twist, (d) <100> STGB, (e) <110> STGB and (f) <111> STGB obtained with four different potentials. The dashed line represents the fitted 1D models for the Basak potential. For all 1D GB sets, the dependence of GB energy on misorientation angle, ξ, is similar for all potentials.

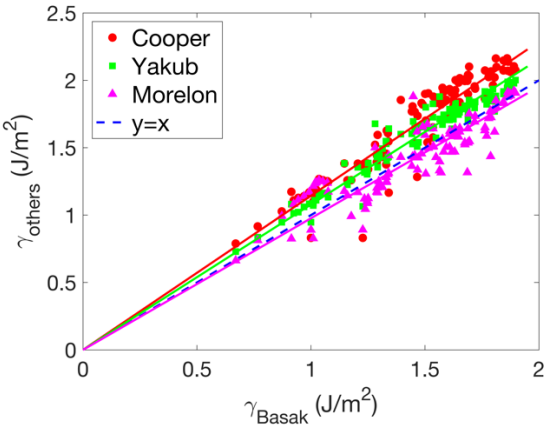

Figure 9. GB energies obtained with Cooper, Yakub, and Morelon potentials versus those obtained with Basak. The MD data are shown by symbols and fitted linearly using $y = ax$, with $a = 1.14$ for Cooper, 1.08 for Yakub, and 0.98 for Morelon, respectively. The dash line plots $y = x$ to guide visualization.

To further show the dependence of interatomic potential, GB energies obtained from the Morelon, Yakub and Cooper potentials are plotted versus those from Basak in Fig. 9. Overall, the Basak and Morelon potentials give similar GBs energies, lower than those from the Cooper and Yakub potentials. The overall linear correlations between the results from different potentials indicate that the present trend on GB energy anisotropy is common across different potentials, although the exact GB energies may vary. There is not sufficient information to conclude which potential is most accurate.

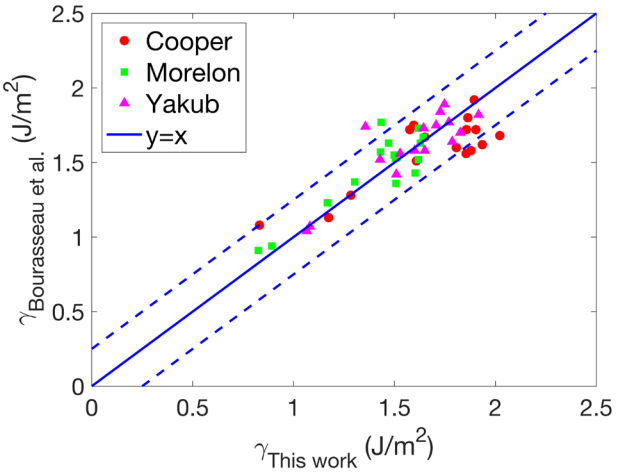

Figure 10. GB energies for selected 1D GBs calculated in this work compared to those from Bourasseau et al. using Cooper, Morelon and Yakub potential. Overall, the agreement is good. The solid line plots $y = x$ and the dash lines $y = x \pm 0.25$, to guide eyes.

4.3 Effect of temperature

Two aspects of the temperature effect are worth discussing. The first is the annealing temperature used in the MD calculation. Here, GBs are annealed at 800 K, which is the same as the temperature used in Nerikar et al. [24], higher than the 300 K in Brutzel et al. [28], but much lower than the 1500 K in Galvin et al. [26], 1870 K in Bourasseau et al. [11] and Ksibi et al. [31], 2000 K in Chen et al. [27], and 3000 K in Williams et al. [29] As shown in Figs 3&4, the GB energies are lower after annealing than at 0 K, and also show a smoother dependence on the misorientation angle, indicating relaxation of the GB structures. To further confirm that the anisotropy observed in the present work is not affected by the annealing temperature used, the results from the current work with the Cooper, Morelon and Yakub potentials are plotted in Fig. 10 versus those in Bourasseau et al. [11] with the same potentials. Only a fraction of the 1D GBs listed in Table 1 are calculated in both this work and Bourasseau et al., where the GBs were annealed at 1870 K for 1 ns. Despite the different annealing temperatures used, good agreement is obtained for all three potentials, particularly for GBs with low energies. Larger differences, mostly within 0.25 J/m^2, are seen for high energy GBs. These errors can be attributed to the omission of γ-surface mapping in Bourasseau et al., the lower annealing temperature used here, and other possible differences in the calculation procedures.

Another possible effect of temperature is on the actual GB structures and energies. GBs at high temperatures may adopt different structures than at low temperatures, e.g., resulting in the so-called GB complexion [49], which is similar to a phase transformation in bulk materials. To date, there has been no evidence of such transition in UO_2. In the absence of such evidence, the GB energy is expected to increase with increasing temperature; however, the GB free energy, which accounts for an entropic contribution, is expected to decrease with increasing temperature [50]. It should be noted that, at finite temperature it is the GB free energy that governs the evolution of GBs and can be experimentally measured. This point needs to be considered while comparing the 0 K results with experimental results, although so far there has been no direct experimental measurement of GB energy in UO_2. Recently, a linear dependence of the average GB energy in UO_2 on temperature has been fitted by Tonks et al. [1] combining atomistic calculations and experimental results. The fitted result at 0 K, 1.56 ± 0.3 J/m^2, agree excellently with the fitted value for random GBs in this work, 1.545 J/m^2.

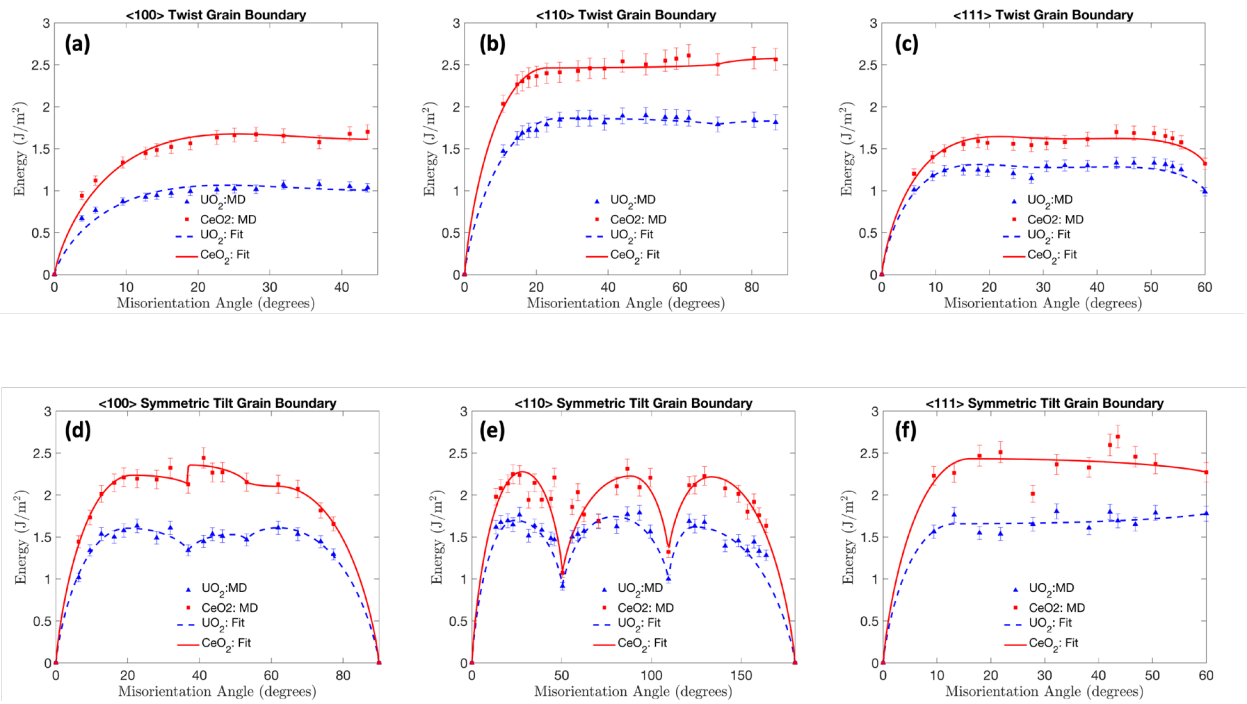

Figure 11. GB energies in CeO_2 versus that in UO_2 (from the Basak potential) for (a) <100> twist, (b) <110> twist, (c) <111> twist, (d) <100> STGB, (e) <110> STGB and (f) <111> STGB. The GBs energies exhibit similar anisotropy in UO_2 and CeO_2.

4.4 Comparison between UO_2 and CeO_2

The above analysis suggests that in UO_2 the GB energy anisotropy is controlled by both the crystal structure and the bonding nature. This implies that the same GB energy anisotropy may exist in other ceramic oxides with similar electronic bonding and fluorite structure. To verify a common GB energy anisotropy, the GB energies in CeO_2, which is frequently used as a surrogate system for studying UO_2, are calculated for the 1D GB sets listed in Table 1.

In Fig.11, the energies of 1D GBs in CeO_2 are plotted as functions of the misorientation angle along with the UO_2 data for comparison. Despite the difference in materials and the independent interatomic potentials used, CeO_2 and UO_2 share a similar dependence of the GB energy on the misorientation angle. Overall, CeO_2 has higher GB energies than UO_2 for the same boundaries. It is also noted that in CeO_2, <100> and <111> twist GBs have similar energies, which is different from UO_2. This indicates that the weight of the ionic interaction on GB energy may vary for different systems.

The similarity of GBs in UO_2 and CeO_2 can be further seen from the correlation between GB energy and GB volume. For both fcc and bcc metals, a correlation between GB energy and excess GB volume has been shown [16,17]. Specifically, high energy GBs tend to have large excess volumes. To verify whether the same correlation exists in UO_2 and CeO_2, the GB volume is plotted versus GB energy in Fig.12 for both materials. For most GBs in UO_2 and CeO_2 considered here, the GB excess volume is in the range from 0.01 to 0.20 a_0, which is higher but not significantly higher than in fcc metals [15]. In general, twist GBs clearly exhibit a positive correlation between

GB volume and GB energy, while such a correlation is less clear for STGBs. Also, twist GBs are observed to have higher GB volume than STGBs. Again, the trends observed in UO_2 and CeO_2 are similar to each other, indicating a general trend for ceramics with the fluorite structure.

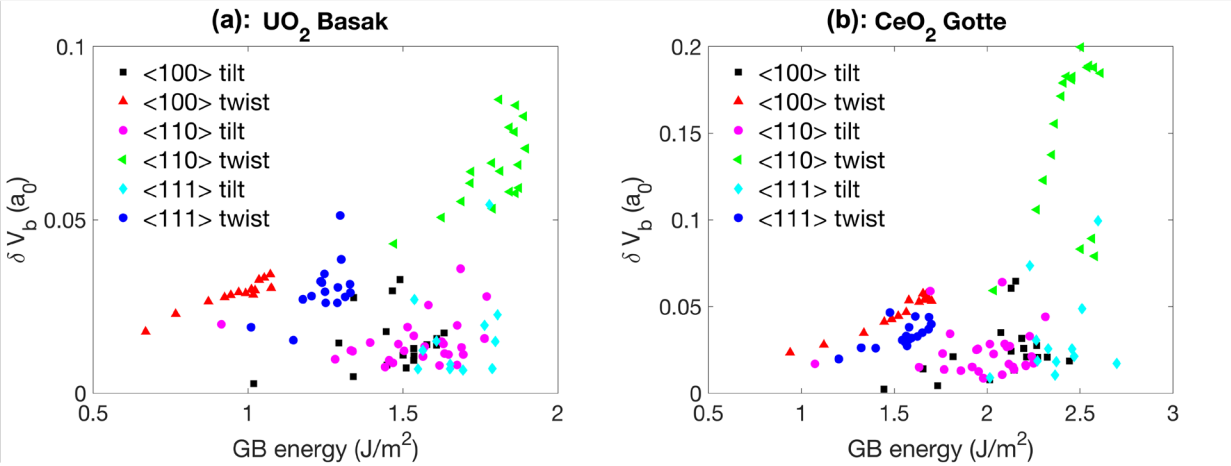

Figure 12. GB excess volume per unit area as a function of GB energy for the 1D GB sets in (a) UO_2 obtained with the Basak potential and (b) in CeO_2 obtained with the Gotte potential. In both materials, positive correlations are seen for twist GBs but not as apparent for tilt GBs.

5. Conclusions

Comprehensive MD calculations are carried out to survey the GB energies in UO_2 and CeO_2 for the purpose of elucidating the roles of crystal structure and bonding nature in affecting GB energy. It is found that the GB energy anisotropy in UO_2 resembles many trends that have been found in fcc metals, implying the influence of the fcc U-sublattice on GB energy. However, it is also found that the GB energy anisotropy is not solely determined by the crystal structure, but also the bonding nature. In UO_2, <111> twist GBs are of higher energy than <100> twist GBs, differing from fcc metals, likely caused by the strong repulsion between ions of the same charge in the GB region. The GB energy anisotropy observed in UO_2 may be general for oxides with the fluorite structure as seen by comparing the UO_2 results with CeO_2.

Acknowledgements

The authors gratefully acknowledge preliminary calculations and foundational efforts contributed by fellow students from Brigham-Young University-Idaho on this project, including Axel Seoane, Chandler Williams, Joseph Carmack, John-Michael Bradley, Emily Togaga'e, Tyler Trogden, William Ireland, Caleb Spear, Eric Sprouse, and Eric Bridenstine.

The authors Zhang and Aagesen thank the DOE NEAMS program for support. The authors Hansen, Harbison, Masengale, and French also express thanks to the Research and Business Development Center and Stephen and Kit Dorrough for support.

Appendix

Table A2 Fitting parameters in the 3D grain boundary energy model for UO_2 using the molecular dynamics results obtained with the Basak potential. The definition and the unit of the parameters are the same as in Bulatov et al. [14].

No.	Name	Description	Value	No.	Name	Description	Value
1	ε_{RGB}	Random boundary energy	1.545	23	$\varepsilon_{110}^{twist,max}$	110 twist energy peak value	1.205
2	d_{100}^{max}	Cutoff distance for 100	0.209	24	$\varepsilon_{110}^{twist,\Sigma3}$	110 twist Σ3	1.158
3	d_{110}^{max}	Cutoff distance for 110	0.016	25	$\varepsilon_{110}^{twist,90}$	110 twist 90 degree (symmetry point)	1.186
4	d_{111}^{max}	Cutoff distance for 111	0.777	26	a_{110}^{atgb}	110 ATGB RSW shape factor	0.494
5	w_{100}^{0}	Weight for 100 set	3.588	27	$\varepsilon_{110}^{stgb,max3}$	110 STGB energy of third peak	1.049
6	w_{110}^{0}	Weight for 110 set	0.968	28	ε_{twin}	110 STGB energy Σ3 (coherent twin)	0.647
7	w_{111}^{0}	Weight for 111 set	5.000	29	$\varepsilon_{110}^{stgb,max2}$	110 STGB energy of second peak	1.129
8	p_{100}^{1}	100 tilt/twist mix power law	0.306	30	$\varepsilon_{110}^{stgb,\Sigma11}$	110 STGB energy Σ11	0.592
9	p_{100}^{2}	100 tilt/twist mix power law	1.173	31	$\varepsilon_{110}^{stgb,max1}$	110 STGB energy of first peak	1.100
10	$\varepsilon_{100}^{twist,max}$	Maximum 100 twist energy	0.651	32	$\pi - \varepsilon_{110}^{stgb,max3}$	110 STGB position of third peak	0.983
11	a_{100}^{twist}	Shape factor for 100 twist	1.429	33	$\pi - \varepsilon_{110}^{stgb,max2}$	110 STGB position of second peak	1.760
12	p	100 ATGB interpolation power law	36.362	34	$\pi - \varepsilon_{110}^{stgb,max1}$	110 STGB position of first peak	2.723
13	$\varepsilon_{100}^{stgb,max1}$	100 STGB energy, first peak	1.039	35	α	111 tilt-twist interpolation	1.793
14	$\varepsilon_{100}^{stgb,\Sigma5,1}$	100 STGB energy, first Σ5	0.868	36	a_{111}^{twist}	111 twist RSW shape factor	1.281
15	$\varepsilon_{100}^{stgb,max2}$	100 STGB energy, second peak	0.990	37	$\xi_{111}^{twist,max}$	111 twist peak angle	0.540
16	$\varepsilon_{100}^{stgb,\Sigma5,2}$	100 STGB energy, second Σ5	0.949	38	$\varepsilon_{111}^{twist,max}$	111 twist energy at peak	0.826
17	$\varepsilon_{100}^{stgb,\Sigma17}$	100 STGB energy, Σ17	1.042	39	$\xi_{111}^{tilt,max}$	111 ATGB peak angle	0.231
18	$\xi_{100}^{stgb,max1}$	100 STGB angle of first peak	0.346	40	$\varepsilon_{111}^{stgb,max}$	111 ATGB maximum energy	1.073
19	$\xi_{100}^{stgb,max2}$	100 STGB angle of second peak	0.857	41	$\varepsilon_{111}^{stgb,\Sigma3}$	111 STGB Σ3 energy	1.151
20	p_{110}^{1}	110 tilt/twist mix power law	0.826	42	$\varepsilon_{111}^{atgb,\Sigma3,max}$	111 ATGB Σ3 symmetry point energy	1.416
21	p_{110}^{2}	110 tilt/twist mix power law	1.006	43	λ	111 ATGB mixing η scale factor	0.100
22	$\xi_{100}^{twist,max}$	110 twist energy peak angle	0.459				

References

[1] M.R. Tonks, P.-C.A. Simon, J. Hirschhorn, Mechanistic grain growth model for fresh and irradiated UO_2 nuclear fuel, J. Nucl. Mater. 543 (2021) 152576.

[2] G. Palumbo, E.M. Lehockey, P. Lin, Applications for grain boundary engineered materials, JOM. 50 (1998) 40–43.
[3] V.V. Rondinella, T. Wiss, The high burn-up structure in nuclear fuel, Mater. Today. 13 (2010) 24–32.
[4] M.R. Tonks, X.-Y. Liu, D. Andersson, D. Perez, A. Chernatynskiy, G. Pastore, C.R. Stanek, R. Williamson, Development of a multiscale thermal conductivity model for fission gas in UO_2, J. Nucl. Mater. 469 (2016) 89–98.
[5] K. Shrestha, T. Yao, J. Lian, D. Antonio, M. Sessim, M.R. Tonks, K. Gofryk, The grain-size effect on thermal conductivity of uranium dioxide, J. Appl. Phys. 126 (2019) 125116.
[6] A. Chernatynskiy, X.-M. Bai, J. Gan, Systematic investigation of the misorientation- and temperature-dependent Kapitza resistance in CeO_2, Int. J. Heat Mass Transf. 99 (2016) 461–469.
[7] M. Oguma, Microstructure Effects on Fracture Strength of UO_2 Fuel Pellets, J. Nucl. Sci. Technol. 19 (1982) 1005–1014.
[8] Y. Zhang, P.C. Millett, M.R. Tonks, X.-M. Bai, S.B. Biner, Molecular dynamics simulations of intergranular fracture in UO_2 with nine empirical interatomic potentials, J. Nucl. Mater. 452 (2014) 296–303.
[9] J. Rest, M.W.D. Cooper, J. Spino, J.A. Turnbull, P. Van Uffelen, C.T. Walker, Fission gas release from UO_2 nuclear fuel: A review, J. Nucl. Mater. 513 (2019) 310–345.
[10] J.A. Turnbull, The Effect of Grain Size on the Swelling and Gas Release Properties of UO_2 During Irradiation, J. Nucl. Mater. 50 (1974), 62-68.
[11] E. Bourasseau, A. Mouret, P. Fantou, X. Iltis, R.C. Belin, Experimental and simulation study of grain boundaries in UO_2, J. Nucl. Mater. 517 (2019) 286–295.
[12] M. Borde, A. Germain, E. Bourasseau, Molecular dynamics study of UO_2 symmetric tilt grain boundaries around [001] axis, J. Am. Ceram. Soc. 104 (2021) 2879–2893.
[13] P.C. Millett, M.R. Tonks, S.B. Biner, L. Zhang, K. Chockalingam, Y. Zhang, Phase-field simulation of intergranular bubble growth and percolation in bicrystals, J. Nucl. Mater. 425 (2012) 130–135.
[14] V.V. Bulatov, B.W. Reed, M. Kumar, Grain boundary energy function for fcc metals, Acta Mater. 65 (2014) 161–175.
[15] D.L. Olmsted, S.M. Foiles, E.A. Holm, Survey of computed grain boundary properties in face-centered cubic metals: I. Grain boundary energy, Acta Mater. 57 (2009) 3694–3703.
[16] D. Wolf, Correlation between structure, energy, and ideal cleavage fracture for symmetrical grain boundaries in fcc metals, J. Mater. Res. 5 (1990) 1708–1730.
[17] D. Wolf, Structure and energy of general grain boundaries in bcc metals, J. Appl. Phys. 69 (1991) 185–196. https://doi.org/10.1063/1.347741.
[18] S. Ratanaphan, D.L. Olmsted, V.V. Bulatov, E.A. Holm, A.D. Rollett, G.S. Rohrer, Grain boundary energies in body-centered cubic metals, Acta Mater. 88 (2015) 346–354.
[19] G.S. Rohrer, Grain boundary energy anisotropy: a review, J. Mater. Sci. 46 (2011) 5881–5895.
[20] D.M. Saylor, A. Morawiec, G.S. Rohrer, The relative free energies of grain boundaries in magnesia as a function of five macroscopic parameters, Acta Mater. 51 (2003) 3675–3686.
[21] L. Helmick, S.J. Dillon, K. Gerdes, R. Gemmen, G.S. Rohrer, S. Seetharaman, P.A. Salvador, Crystallographic Characteristics of Grain Boundaries in Dense Yttria-Stabilized Zirconia, Int. J. Appl. Ceram. Technol. 8 (2011) 1218–1228.
[22] G.S. Rohrer, The distribution of grain boundary planes in polycrystals, JOM. 59 (2007) 38–42.

[23] W.T. Read, W. Shockley, Dislocation Models of Crystal Grain Boundaries, Phys. Rev. 78 (1950) 275–289.
[24] P.V. Nerikar, K. Rudman, T.G. Desai, D. Byler, C. Unal, K.J. McClellan, S.R. Phillpot, S.B. Sinnott, P. Peralta, B.P. Uberuaga, C.R. Stanek, Grain Boundaries in Uranium Dioxide: Scanning Electron Microscopy Experiments and Atomistic Simulations, J. Am. Ceram. Soc. 94 (2011) 1893–1900.
[25] K. Rudman, P. Dickerson, D. Byler, R. McDonald, H. Lim, P. Peralta, C. Stanek, K. McClellan, Three-Dimensional Characterization of Sintered UO_{2+x}: Effects of Oxygen Content on Microstructure and Its Evolution, Nucl. Technol. 182 (2013) 145–154.
[26] C.O.T. Galvin, M.W.D. Cooper, P.C.M. Fossati, C.R. Stanek, R.W. Grimes, D.A. Andersson, Pipe and grain boundary diffusion of He in UO_2, J. Phys. Condens. Matter. 28 (2016)
[27] T. Chen, D. Chen, B.H. Sencer, L. Shao, Molecular dynamics simulations of grain boundary thermal resistance in UO_2, J. Nucl. Mater. 452 (2014) 364–369.
[28] L.V. Brutzel, E. Vincent-Aublant, Grain boundary influence on displacement cascades in UO_2: A molecular dynamics study, J. Nucl. Mater. 377 (2008) 522–527.
[29] N.R. Williams, M. Molinari, S.C. Parker, M.T. Storr, Atomistic investigation of the structure and transport properties of tilt grain boundaries of UO_2, J. Nucl. Mater. 458 (2015) 45–55.
[30] X.-M. Bai, Y. Zhang, M.R. Tonks, Testing thermal gradient driving force for grain boundary migration using molecular dynamics simulations, Acta Mater. 85 (2015) 95–106.
[31] A. Ksibi, E. Bourasseau, X. Iltis, D. Drouan, M. Gaudet, A. Germain, A. Pena, G. Lapertot, J.-P. Brison, R.C. Belin, Experimental and numerical assessment of grain boundary energies in polycrystalline uranium dioxide, J. Eur. Ceram. Soc. 40 (2020) 4191–4201.
[32] E.R. Homer, S. Patala, J.L. Priedeman, Grain Boundary Plane Orientation Fundamental Zones and Structure-Property Relationships, Sci. Rep. 5 (2015) 15476.
[33] H. Grimmer, W. Bollmann, D.H. Warrington, Coincidence-site lattices and complete pattern-shift in cubic crystals, Acta Crystallogr. Sect. A. 30 (1974) 197–207.
[34] C.B. Basak, A.K. Sengupta, H.S. Kamath, Classical molecular dynamics simulation of UO_2 to predict thermophysical properties, J. Alloys Compd. 360 (2003) 210–216.
[35] N.-D. Morelon, D. Ghaleb, J.-M. Delaye, L. Van Brutzel, A new empirical potential for simulating the formation of defects and their mobility in uranium dioxide, Philos. Mag. 83 (2003) 1533–1555.
[36] E. Yakub, C. Ronchi, D. Staicu, Molecular dynamics simulation of premelting and melting phase transitions in stoichiometric uranium dioxide, J. Chem. Phys. 127 (2007) 094508.
[37] M.W.D. Cooper, M.J.D. Rushton, R.W. Grimes, A many-body potential approach to modelling the thermomechanical properties of actinide oxides, J. Phys. Condens. Matter. 26 (2014) 105401.
[38] K. Yamada, K. Kurosaki, M. Uno, S. Yamanaka, Evaluation of thermal properties of uranium dioxide by molecular dynamics, J. Alloys Compd. 307 (2000) 10–16.
[39] A. Chernatynskiy, C. Flint, S.B. Sinnott, S.R. Phillpot, Critical assessment of UO_2 classical potentials for thermal conductivity calculations, J. Mater. Sci. 47 (2012) 7693–7702.
[40] K. Govers, S. Lemehov, M. Hou, M. Verwerft, Comparison of interatomic potentials for UO_2. Part I: Static calculations, J. Nucl. Mater. 366 (2007) 161–177.
[41] D. Wolf, P. Keblinski, S.R. Phillpot, J. Eggebrecht, Exact method for the simulation of Coulombic systems by spherically truncated, pairwise r^{-1} summation, J. Chem. Phys. 110 (1999) 8254–8282.

[42] Y. Zhang, X.-Y. Liu, P.C. Millett, M. Tonks, D.A. Andersson, B. Biner, Crack tip plasticity in single crystal UO_2: Atomistic simulations, J. Nucl. Mater. 430 (2012) 96–105.
[43] S. Plimpton, Fast Parallel Algorithms for Short–Range Molecular Dynamics, Journal of Computational Physics 117, 1-19 (1995).
[44] W. Shinoda, M. Shiga, M. Mikami, Rapid estimation of elastic constants by molecular dynamics simulation under constant stress, Phys. Rev. B. 69 (2004) 134103.
[45] A. Stukowski, Visualization and analysis of atomistic simulation data with OVITO–the Open Visualization Tool, Model. Simul. Mater. Sci. Eng. 18 (2010) 015012.
[46] A. Gotte, D. Spangberg, K. Hermansson, M. Baudin, Molecular dynamics study of oxygen self-diffusion in reduced CeO_2, Solid State Ion. 178 (2007) 1421–1427.
[47] D. Wolf, A read-shockley model for high-angle grain boundaries, Scr. Metall. 23 (1989) 1713–1718.
[48] S. Ratanaphan, R. Sarochawikasit, N. Kumanuvong, S. Hayakawa, H. Beladi, G.S. Rohrer, T. Okita, Atomistic simulations of grain boundary energies in austenitic steel, J. Mater. Sci. 54 (2019) 5570–5583.
[49] P.R. Cantwell, M. Tang, S.J. Dillon, J. Luo, G.S. Rohrer, M.P. Harmer, Grain boundary complexions, Acta Mater. 62 (2014) 1–48.
[50] B. Beeler, M. Baskes, D. Andersson, M.WD. Cooper, Y. Zhang, Molecular dynamics investigation of grain boundaries and surfaces in U_3Si_2, J. Nucl. Mater. 514 (2019) 290–298.